nature geoscience
SUPPLEMENTARY INFORMATION
DOI: 10.1038/NGEO1857

Volcanic subsidence triggered by the 2011 Tohoku earthquake in Japan

Supplementary Information

1. Acquisition and processing of ALOS/PALSAR images

This project is affiliated with the Earthquake Working Group for the Evaluation of ALOS for Use in Disaster Mitigation, led by the Japan Aerospace Exploration Agency (JAXA). JAXA conducted emergency observations with PALSAR immediately after the 2011 Tohoku earthquake. Strip-map mode observations of the northeastern half of Honshu Island were made from six ascending orbits (paths 400–405, with an off-nadir angle of 34.3º) and three descending orbits (paths 56 and 59 with an off-nadir angle of 34.3º, path 58 with an off-nadir angle of 28.8º). Owing to an issue with the power supply system, the satellite stopped acquiring data on 22 April 2011, and JAXA announced the termination of its operation on 12 May 2011. Therefore, images were acquired only once per path after the earthquake.

The interferometric synthetic aperture radar (InSAR) technique uses two SAR images to measure displacements in the radar's look (line-of-sight; LOS) direction that occurred between the acquisition times. For each path from which an image was acquired after the Tohoku earthquake, we used another image acquired before the earthquake to perform InSAR analysis (Supplementary Table 1, Supplementary Fig. 1). Because the satellite terminated its operation before acquiring images in the target areas from the descending orbits, we used only the interferograms computed from the images acquired from the ascending orbits. For all these ascending interferograms, the PALSAR radar incidence angle was approximately 39° and the horizontal component of the LOS vector was inclined 80° eastward from north. Therefore, the measurements are most sensitive to ground displacements in the vertical and E–W directions. We applied two-pass differential interferometry to the image pairs using the GAMMA® software with the digital elevation models (DEMs) made available by the Consultative Group on International Agricultural Research[1]. These elevation models were created by filling holes in those created by the Shuttle Radar Topography Mission. The interferograms were averaged for pixel windows of 80 m × 80 m (later averaged to 800 m × 800 m windows) and further denoised using a spectrum filter with a parameter of 0.5 and a window size of 64 pixels[2]. The interferograms mainly show coherent phase changes due to the Tohoku earthquake (Supplementary Fig. 1). The patterns are concentric, centred at the epicentre of the quake. The maximum LOS displacement was 3.6 m, obtained from an ascending orbit.

Disturbance in the interferometric fringes can be recognized around the five volcanoes targeted in this study (Supplementary Fig. 2), reflecting the presence of local signals. To extract these subtle signals, the phase changes due to the Tohoku earthquake rupture must be removed. These coseismic phase changes were removed by subtracting low-pass filtered interferograms from the originals. For Figures 1b–e and deformation modelling, the local deformation signals were extracted more accurately in the following manner. Because interferograms usually contain tropospheric phase artefacts correlated with the altitude, we also simultaneously removed the phase component proportional to the altitude.

(1) An interferogram is cropped in a region surrounding the target area.

(2) The cropped interferogram is further multilooked (averaged to 800 m × 800 m windows) and low-pass filtered.

(3) The filtered interferogram is unwrapped using the SNAPHU software[3], with the decorrelated areas masked.

(4) The unwrapped interferogram is downsampled by selecting one data point from every three points. Here, data points located in the target area (locally deformed area) are not selected.

(5) The phase components that can be approximated by a second-order polynomial in both the latitude and longitude directions and the component proportional to the altitude are estimated by a least squares method. The former corresponds primarily to the coseismic deformation of the Tohoku earthquake and the latter to tropospheric phase artefacts.

(6) The estimated phase components are simulated on the grid of the original interferogram.

(7) The simulated phase is subtracted from the original interferogram to obtain localized signals.

2. Verification of tropospheric artefacts

The principal component of the tropospheric artefacts is correlated with the altitude[4,5]. However, with the exception of Mt. Zao, the obtained signals are poorly correlated with the altitude (Supplementary Fig. 3), suggesting that the obtained signals are real. As explained in the main text, the subsidence at Mt. Zao is validated by GPS data; hence, the reliability of the Mt. Zao signal is high. Each of the deformed areas was captured by two independent interferograms (Supplementary Table 2). The fact that the signals obtained from two different paths are similar (Supplementary Fig. 3) implies a common origin of the phase change, further supporting the possibility of deformation rather than tropospheric artefacts that are generally random. An isolated signal to the northwest of Mt. Zao in Figure 1c (marked with a black circle) corresponds to the phase difference in the 4th column of Supplementary Figure 3. Thus, this signal can be regarded as a tropospheric artefact. In the modelling, we chose one of the two interferograms for each target on the basis of two criteria: (1) the target area coverage and (2) the signal-to-noise ratio (fewer atmospheric artefacts, higher coherence).

3. GPS data processing

For Mt. Zao and Mt. Azuma, stations of the nationwide GPS Earth Observation Network (GEONET), installed and maintained by the Geospatial Information Authority of Japan (GSI), were located in the deformed zones (Fig. 1). We analysed the daily coordinates published by the GSI to verify the subsidence. For Mt. Zao and Mt. Azuma, we could examine the displacements at GPS stations located inside the area of the InSAR subsidence signal. First, we converted the latitude and longitude coordinates into local kilometric coordinates in order to obtain displacement time series in the eastward, northward and vertical directions. This resulted mainly in obtaining the coseismic displacements of the Tohoku earthquake. Then, the displacements obtained outside the InSAR signal zone were subtracted from those obtained inside the zone (Supplementary Fig. 4). Finally, a moving average with a three-day time window was taken to reduce noise. The result (Fig. 2) shows that the points located in the InSAR signal zones indeed subsided. We also examined 30-second sampling displacement time-series obtained from kinematic GPS analysis, but they were too noisy to judge if the subsidence accompanied transient of a few to several hours or not.

We further examined the spatial distribution of the GPS-derived subsidence in detail, whose results are displayed in Fig. 1d and e. First, we subtracted the coseismic GPS displacements calculated by the fault model[6] from those observed by GEONET. Next, we modelled the residual vector fields using a bicubic polynomial function and subtracted the modelled trend from the residual vectors. Finally, the detrended GPS displacements thus obtained were projected into the LOS direction of InSAR. The results (coloured circles in Figs. 1d and e) are comparable to InSAR observations, indicating that the InSAR signals obtained at Mt. Zao and Mt. Azuma are not artefacts (except for an isolated signal in Fig. 1c, marked with a black circle).

4. Volcanoes in northeastern Honshu

According to the definition of the Japan Meteorological Agency (JMA)[7], there are 18 active volcanoes (i.e. those that erupted less than 10,000 years ago) in northeastern (Tohoku) Honshu. While many of these volcanoes exhibit geothermal and fumarole activity, eruptions occur only occasionally. The last eruption that occurred in northeastern Honshu with a volcanic explosivity index (VEI) of >2 was in 1971 at Akitakoma[7], although clear seismic unrest and deformation were evidenced at the Onikobe caldera (~20 km SSW of the summit of Mt. Kurikoma, Fig. 1c) in 1996[8] and at Mt. Iwate, approximately 20 km northeast of the summit of Mt. Akitakoma (Fig. 1b), in 1998[9].

The change in activity observed during/after the occurrence of the Tohoku earthquake is summarized in Supplementary Table 3. No drastic change was observed at these volcanoes in association with the megathrust quake, except at Mt. Akitakoma, which experienced intensified seismic activity beneath the summit.

The subsided regions are not only closest to the earthquake rupture area but also exhibit high geothermal activities. The regions generally show high geothermal gradient (Fig. 3a) and high temperature of thermal water (Fig. 3b). These data as well as concentrations of Late Cenozoic calderas indicate that massive plutons are present beneath these regions.

To check the deformation of the target volcanoes prior to the Tohoku earthquake, we computed a total of 196 ALOS/PALSAR interferograms of the volcanoes targeted in this study, excluding Mt. Nasu, for which we only had the pairs that span the Tohoku earthquake. We found no clear deformation signals from June 2006 until the occurrence of the earthquake in the four target regions. On interferograms for Mt. Zao and Mt. Azuma, which used the image acquired on 6 June 2006, we found phase change patterns that appear somewhat similar to those obtained in this study. However, the GPS displacements do not indicate any deformation during the corresponding periods (Supplementary Fig. 5); hence, these phase changes are likely to originate from the troposphere.

5. Inversion procedure for the source of subsidence

Based on our hypothesis that a highly deformable region should lie beneath the subsided ground, we modelled the sources of subsidence as a triaxial ellipsoid with zero tangential and normal traction over its surface. This boundary condition indicates the effect of the inclusion of very low-strength material that strongly disturbs the external stress field. These model computations were conducted for the volcanoes that exhibited relatively simple subsidence patterns, i.e. Mt. Akitakoma, Mt. Azuma (explained in the main text) and Mt. Nasu.

We used a mixed boundary element method (BEM)[10] to compute ground displacements due to the deformation of the ellipsoid. Under the assumptions of linear, homogeneous and isotropic elasticity, the mixed BEM method allows computation of the deformation caused by a stress change exerted on the surface of the ellipsoid and the resulting displacements on the ground surface. The method considers the realistic topography. Schematic figures explaining the boundary conditions on the surface of the ellipsoid are given in Supplementary Figure 6. The strain changes at the sites were computed from the fault model, which consists of a set of finite rectangular dislocations for the mainshock and the largest aftershock that occurred 30 minutes after the mainshock[6] (Supplementary Fig. 7); these strain changes were subsequently converted to stress changes using prescribed elastic constants. The Markov chain Monte Carlo (MCMC) method was used to search for models that explained the observations well. The MCMC method samples the model space in such a way that the density of the points eventually becomes proportional to the probability density function of the model parameters, allowing us to not only obtain the optimum (maximum likelihood) model but also estimate model uncertainties.

The data to be used in the inversions were prepared in the following manner. First, the interferograms were transformed into local kilometric coordinates with the centre of the deformed area set as the origin; they were then low-pass filtered, phase unwrapped (converted from phase to LOS displacements) and subsampled in concentric grids (Supplementary Fig. 8, left column). Subsampling was conducted such that the density of the data points became smaller at areas further from the deformation centre. This concentric subsampling method has been shown to not bias model results for similar problems[11,12]. Areas where signals were decorrelated or considered to be artefacts were not used. The numbers of subsampled points were 485 (Mt. Akitakoma), 431 (Mt.

Azuma) and 571 (Mt. Nasu).

We assumed that the data could be explained adequately by a model consisting of 10 parameters (Supplementary Table 4). The location of the ellipsoid is specified by three parameters: the easting and northing of the centre of the ellipsoid and the elevation of the top of the ellipsoid. We did not use the elevation of the centre of the ellipsoid to avoid unrealistic location of the source such that the ellipsoid penetrates the ground surface. The geometry of the ellipsoid is specified by four parameters. It is assumed here that the two ellipsoidal axes are in the horizontal plane and the third axis is in the vertical plane. We adopted the strike angle of the major horizontal axis, the length of the major horizontal axis, the length of the minor horizontal axis with respect to the major horizontal axis and the length of the vertical axis with respect to the major horizontal axis as model parameters.

In addition to the geometrical parameters explained above, we introduced three nuisance parameters: apparent displacement offset and apparent displacement trends in both the east and north directions. The offset is required because InSAR data are not referenced to any point. We decided to estimate the displacement trends even if such trends should have been removed by the detrending explained in the first section of the Supplementary Information, because there may be some residual trend localized in the deformed areas.

The Young's modulus and the Poisson's ratio were assumed to be 20 GPa and 0.25, respectively. The Poisson's ratio was obtained from the ratio of the P and S wave velocities in the Tohoku region[13]. To obtain the Young's modulus, we further assumed a host rock density of 2500 kg/m^3 and a static to dynamic ratio of 0.3[14]. The static to dynamic ratio is generally a function of the porosity[14] and its value in the crust is poorly known. For this reason, we tested inversions with different Young's modulus; for the range 10–30 GPa, the results were qualitatively the same except for slight systematic differences in the depth of the top of the ellipsoid (approximately 250 m deeper for the 30 GPa case than for the 10 GPa case) and in the volume of the ellipsoid (approximately 15% larger for the 30 GPa case than for the 10 GPa case). Therefore, our results are robust in terms of the uncertainty in the assumed Young's modulus.

As evidence of fluid migration has not been found, we did not assume any pressure change over the surface of the ellipsoid as a result of the Tohoku earthquake. We confirmed by supplementary inversions that the subsidence signals could also be explained solely by a pressure decrease rather than by the stress changes due to the Tohoku earthquake, indicating that we cannot exclude the possibility that the cause of the subsidence is such a pressure decrease.

We used a likelihood function defined as

$$L(\mathbf{m}) = \exp[-(\mathbf{u}_{\boldsymbol{o}} - \mathbf{u}_{\boldsymbol{m}})^T \mathbf{C}_d^{-1} (\mathbf{u}_{\boldsymbol{o}} - \mathbf{u}_{\boldsymbol{m}})], \qquad \text{(S1)}$$

where $\mathbf{u}_{\boldsymbol{o}}$ and $\mathbf{u}_{\boldsymbol{m}}$ represent the observed and modelled displacements, respectively. The modelled displacements of one realization include those predicted from a boundary element computation $\mathbf{u}_{\boldsymbol{BEM}}$ as well as the apparent displacement offset and trends. Namely,

$$\mathbf{u}_{\boldsymbol{m}} = \mathbf{u}_{\boldsymbol{BEM}} + a + b\mathbf{x} + c\mathbf{y}, \qquad \text{(S2)}$$

where (x_i, y_i) corresponds to (easting, northing) of the *i*-th data point, and constants a, b and c are model parameters to be estimated. The data covariance matrix $\mathbf{C}_d^{-1}$ accounts for the uncertainties in the observed displacements and their correlation. We assumed that the data noise follows an exponential correlation function. The (*i*,*j*) element of the covariance matrix can be written as

$$C_{dij} = \sigma_d^2 \exp(-\frac{r_{ij}}{a}), \quad \text{(S3)}$$

where σ_d^2 is the data variance, a is the correlation length, and r_{ij} is the distance between the i-th and j-th data points. To determine the variance σ_d^2 and correlation length a, we computed the autocorrelation functions of the residual $\mathbf{u_o}$–$\mathbf{u_m}$ of some preliminary inversions, from which we obtained $\sigma_d^2 \approx 0.01^2$ m^2 and $a \approx 3000$ m. These values were used for all the inversions.

For each realization of forward computation, the mesh of the triaxial ellipsoid was generated, the LOS ground displacements were computed by the BEM, and the likelihood function (eq. (S1)) was evaluated. For each MCMC inversion, iterations of 60,000 forward computations were made. We retained the sample every three steps and discarded other samples. The resulting 20,000 samples were used to evaluate the posterior probability density (PPD) functions of the model space. We confirmed that the shapes of the PPD functions did not change as the number of samples was further increased, indicating that 20,000 samples are sufficient to evaluate the probability density functions for this type of problem.

6. Inversion results

The comparisons of subsampled data and predictions from the optimum models are shown in Supplementary Figure 8. The observed displacements are explained fairly well by the optimum models. A small amount of systematic residuals remains for Mt. Akitakoma, indicating a more complex shape of the deformable region than assumed. The sidewalls facing the principal axis direction of the tensional stress change are pulled outwards, whereas the top wall is pulled downwards (Supplementary Fig. 9). We computed the 95% confidence intervals of the model parameters from one-dimensional marginal PPDs (see Supplementary Fig. 10 for an example). The confidence intervals (Supplementary Table 5) indicate that the depth of the top of the ellipsoid should be shallower than a few kilometres for both Mt. Akitakoma and Mt. Azuma. The depth for Mt. Nasu is poorly constrained. It should be noted that the ground subsidence is sensitive only to the upper side of the deformation source (ellipsoid) and the vertical dimension of the source (length of the vertical axis for our ellipsoidal model) is generally poorly constrained (Supplementary Table 5).

References

1) Jarvis, A., Reuter, H. I., Nelson, A. & Guevara, E. Hole-filled SRTM data V4. International Centre for Tropical Agriculture (CIAT), http://www.srtm.csi.cgiar.org (2008).
2) Goldstein, R. M. & Werner, C. L. Radar interferogram filtering for geophysical applications. *Geophys. Res. Lett.* **25**, 4035-4038 (1998).
3) Chen, C. W. & Zebker, H. A. Network approaches to two-dimensional phase unwrapping: Intractability and two new algorithms. *J. Opt. Soc. Am.* **17**, 401-414 (2000), doi:10.1364/JOSAA.17.000401.
4) Beauducel, F., Briole, P. & Froger, J.-L. Volcano-wide fringes in ERS synthetic aperture radar interferograms of Etna (1992-1998): Deformation or tropospheric effect?. *J. Geophys. Res.*, **105**, 16, 391-16,402 (2000).
5) Onn, F. & Zebker, H. A. Correction for interferometric synthetic aperture radar atmospheric phase artefacts using time series of zenith wet delay observations from a GPS network, *J. Geophys. Res.* **111**, B09102 (2006),

doi:10.1029/2005JB004012.

6) Nishimura, T., Munekane, H. & Yarai, H. The 2011 off the Pacific coast of Tohoku Earthquake and its aftershocks observed by GEONET. *Earth Planets Space* **63**, 631-636 (2011).

7) Japan Meteorological Agency (2005), National Catalogue of the active volcanoes in Japan (3rd edition).

8) Takada, Y. & Furuya, M. Aseismic slip during the 1996 earthquake swarm in and around the Onikobe geothermal area, NE Japan. *Earth Planet. Sci. Lett.* **290**, 302-310 (2010), doi:10.1016/j.epsl.2009.12.024.

9) Nishimura, T. *et al*. The M6.1 earthquake triggered by volcanic inflation of Iwate Volcano, northern Japan, observed by satellite radar interferometry. *Geophys. Res. Lett*. **28**, 635-638 (2001).

10) Cayol, V. & Cornet, F. H. 3-D mixed boundary elements for elastostatic deformation field analysis. *Int. J. Rock Mech. Min. Sci*. **34**, 275-287 (1997).

11) Fukushima, Y., Cayol, V. & Durand, P. Finding realistic dike models from interferometric synthetic aperture radar data: the February 2000 eruption at Piton de la Fournaise. *J. Geophys. Res.* **110**, B03206 (2005), doi:10.1029/ 2004JB003268.

12) Fukushima, Y., Mori, J., Hashimoto, M. & Kano, Y. Subsidence associated with the LUSI mud eruption, East Java, investigated by SAR interferometry. *Mar. Petrol. Geol.* **29**, 1740-1750 (2009), doi:10.1016/j.marpetgeo.2009.02.001.

13) Tsuji, Y., Nakajima, J. & Hasegawa, A. Tomographic evidence for hydrated oceanic crust of the Pacific slab beneath northeastern Japan: Implications for water transportation in subduction zones. *J. Geophys. Res.* **35**, L14308 (2008).

14) Cheng, C. H. & Johnston, D. H. Dynamic and static moduli. *Geophys. Res. Lett.* **8**, 39-42 (1981).

15) Coordinating Committee for Prediction of Volcanic Eruption, 2011, Report issued at the 120th meeting of the committee, 7 June 2011 (http://www.seisvol.kishou.go.jp/tokyo/STOCK/kaisetsu/CCPVE/shiryo/120/120_no05.pdf, in Japanese).

Supplementary Table 1. List of the ALOS/PALSAR images used in this study

Path	Orbit	Master YY/MM/DD	Slave YY/MM/DD	Bperp[a] (m)	Incidence Angle[a] (deg)
401	Ascending	10/28/10	11/03/15	1465	38.7
402	Ascending	10/09/29	11/04/01	1199	38.7
403	Ascending	11/03/03	11/04/18	360	38.7
404	Ascending	11/02/02	11/03/20	829	38.7
405	Ascending	11/02/19	11/04/06	407	38.7

[a] The perpendicular baselines (Bperp) and incidence angles are the values at the scene centre.

Supplementary Table 2. Target regions and data that captured deformation

	Used in modelling and Figs. 1b–f	Other data that captured deformation
Akitakoma	Path 402	Path 403
Kurikoma	Path 403	Path 402
Zao	Path 404	Path 403
Azuma	Path 404	Path 405
Nasu	Path 405	Path 404

Supplementary Table 3. Change in the activity of selected volcanoes in eastern Honshu at the time of occurrence of the Tohoku earthquake, summarized from a report by the JMA[15]

	Fumarole/Geo-thermal activity	Seismicity	Deformation other than the coseismic effect of the Tohoku earthquake
Iwate	Continuation of low-level fumarole activity	Slight increase in the number of shallow volcanotectonic earthquakes	No clear deformation detected
Akitakoma	Continuation of fumarole activity	Slight increase in the number of shallow volcanotectonic earthquakes	No clear deformation detected
Kurikoma	No activity	No change	No clear deformation detected
Zao	No activity	No change	No clear deformation detected
Azuma	Continuation of fumarole activity	Slight increase in shallow volcanic earthquakes	GPS measurements around the summit in two periods (Oct. 2010 and May 2011) show contraction of the summit area between the two periods
Bandai	Continuation of low-level fumarole activity	No change	No clear deformation detected
Nasu	Continuation of low-level fumarole activity	No change	No clear deformation detected

Supplementary Table 4. Parameters and their search range

Parameters†	Unit	Search Range
Easting with respect to an arbitral origin (East)	m	[−15,000, 15,000]
Northing with respect to an arbitral origin (North)	m	[−15,000, 15,000]
Elevation of the top of the ellipsoid (Top)	m	[−10,000, 2000]
Strike angle of S1 measured from North	deg	[−90, 90] (all directions)
S1* (S1)	m	[1000, 25,000]
S2/S1* (S2r)		[0.1, 1.0]
S3/S1* (S3r)		[0.1, 5.0]
Displacement offset (Offs)	cm	[−10, 10]
Displacement trend along the longitude (TrendX)	10^{-6} m/deg	[−20, 20]
Displacement trend along the latitude (TrendY)	10^{-6} m/deg	[−20, 20]

† Abbreviated names are given in parentheses.

* S1: Length of the horizontal major axis, S2: length of the horizontal minor axis, S3: length of the vertical axis

Supplementary Table 5. Confidence intervals

Parameters*	Akitakoma			Azuma			Nasu		
	Min.	Optimum	Max.	Min.	Optimum	Max.	Min.	Optimum	Max.
East (m)	−1667	668	2576	−1667	−22	1667	−4697	−896	2576
North (m)	1061	7861	8636	1061	3119	5303	−5909	2313	9242
Top (m)	−4818	−1820	−1485	−2364	−1260	−182	−9515	−3838	-1273
Strike (deg)	−21	−17	133	−34	−20	−1	UC†	−12	UC†
S1 (m)	13,363	20,342	21,121	9242	11,720	14,091	8273	12,729	23,545
S2/S1	0.69	0.68	1.00	0.34	0.48	0.72	0.28	0.64	1.00
S3/S1	0.35	0.64	1.34	0.35	0.56	1.34	0.50	0.46	3.86
Offs (cm)	−0.07	0.62	1.48	−0.64	0.52	1.06	−0.91	0.10	2.32
TrendX (10^{-6} m/deg)	0.24	0.70	1.02	1.34	2.30	3.04	−1.41	0.94	2.62
TrendY (10^{-6} m/deg)	−0.89	−0.62	−0.11	−0.78	0.15	0.78	−1.82	0.27	2.22

* Refer to Supplementary Table 4 for the meanings of the parameters.

† Unconstrained. This means that the major horizontal axis can be in any direction.

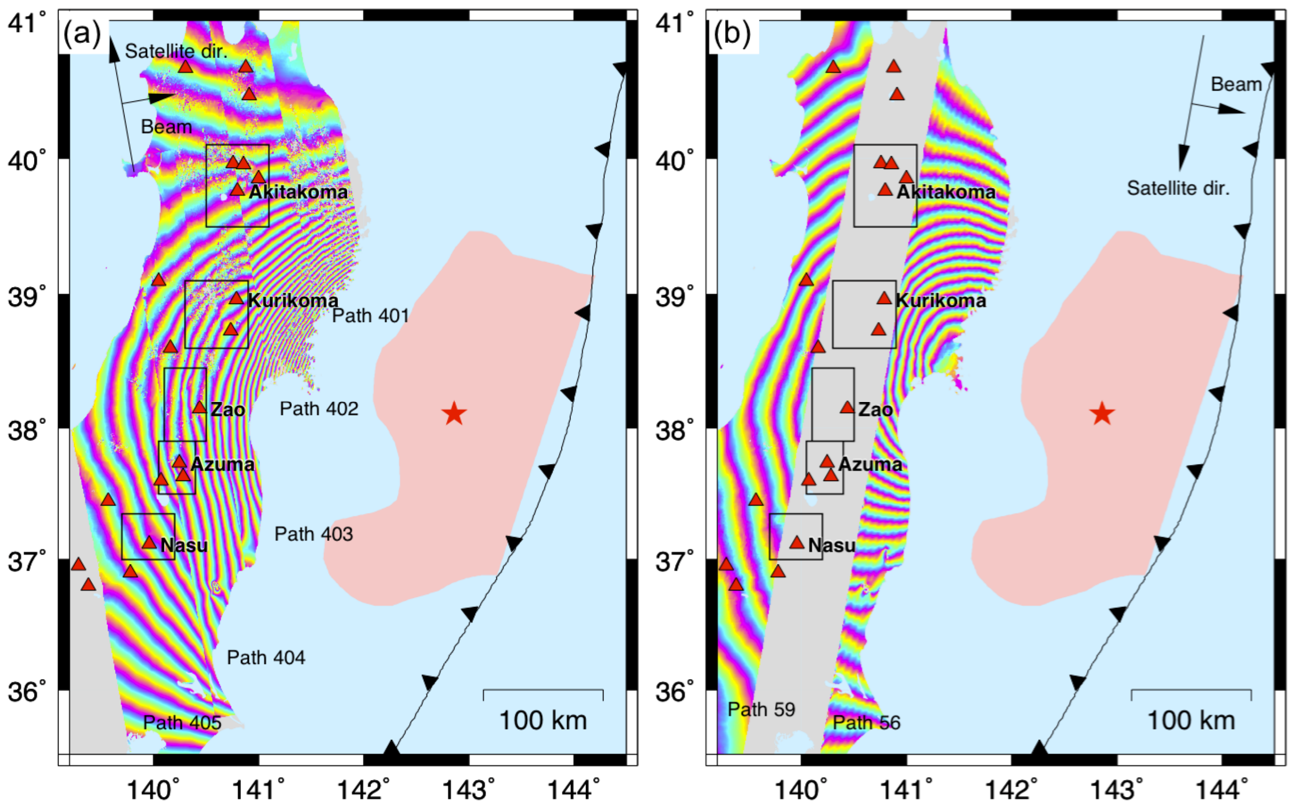

Supplementary Fig. 1. Interferograms obtained by processing PALSAR images acquired from ascending (a) and descending (b) orbits. The images acquired before and after the occurrence of the Tohoku earthquake were used. Refer to Fig. 1 for the legends.

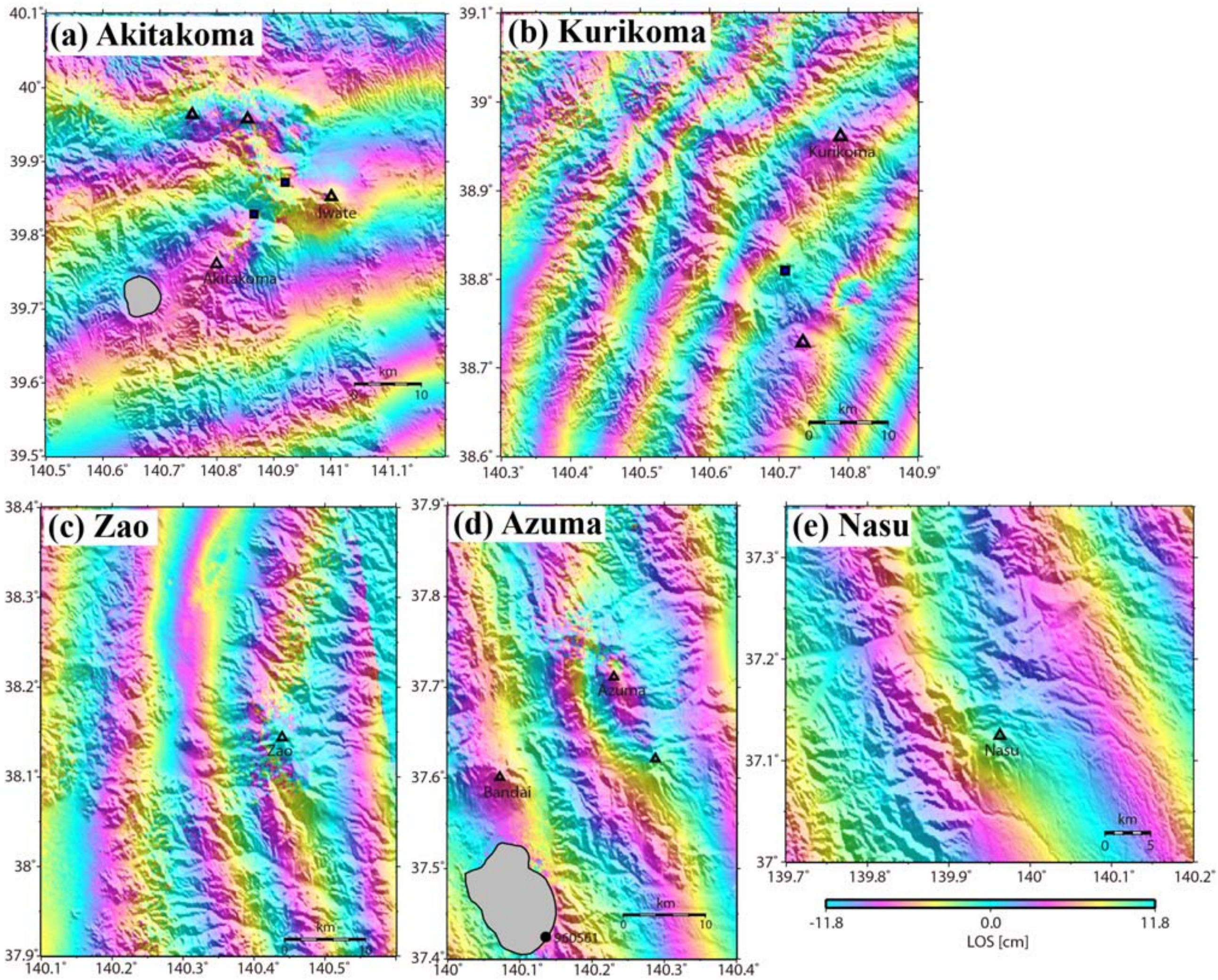

Supplementary Fig. 2. Interferograms around the subsided volcanic regions without removal of the fringes due to the Tohoku earthquake rupture. Refer to Fig. 1 for legends. Black filled circle in (d) labeled 960561 is the reference GEONET station used in Fig. 2a and Supplementary Fig.4a.

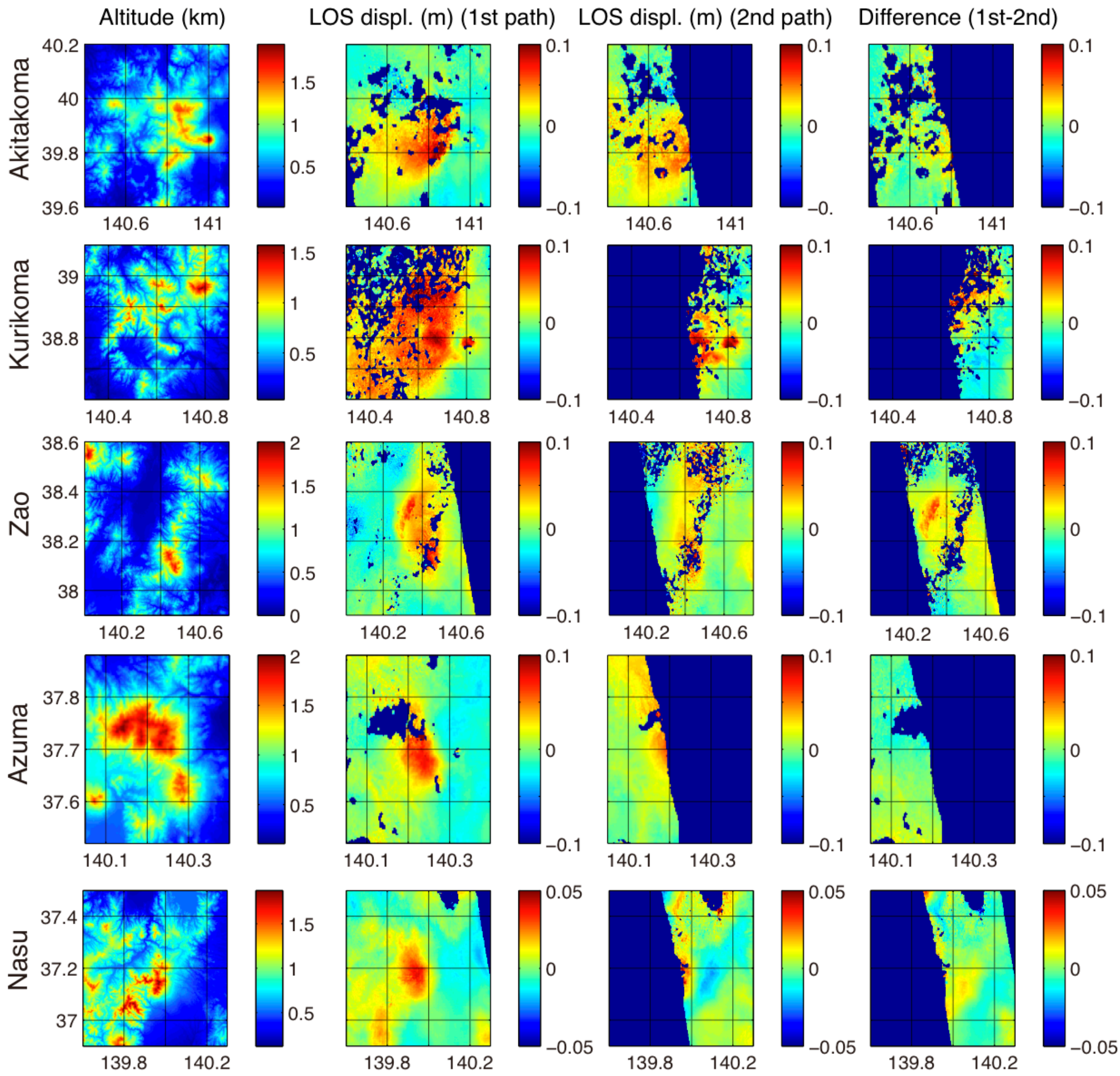

Supplementary Fig. 3. Comparison of the terrain altitude (1st column), the unwrapped and detrended InSAR LOS displacements from two different paths (2nd and 3rd columns), and the difference of the displacements observed from the two paths (4th column) for the five volcanic regions. Decorrelated areas and those out of the data strips are shown in dark blue. The two paths for each region are listed in Supplementary Table 2.

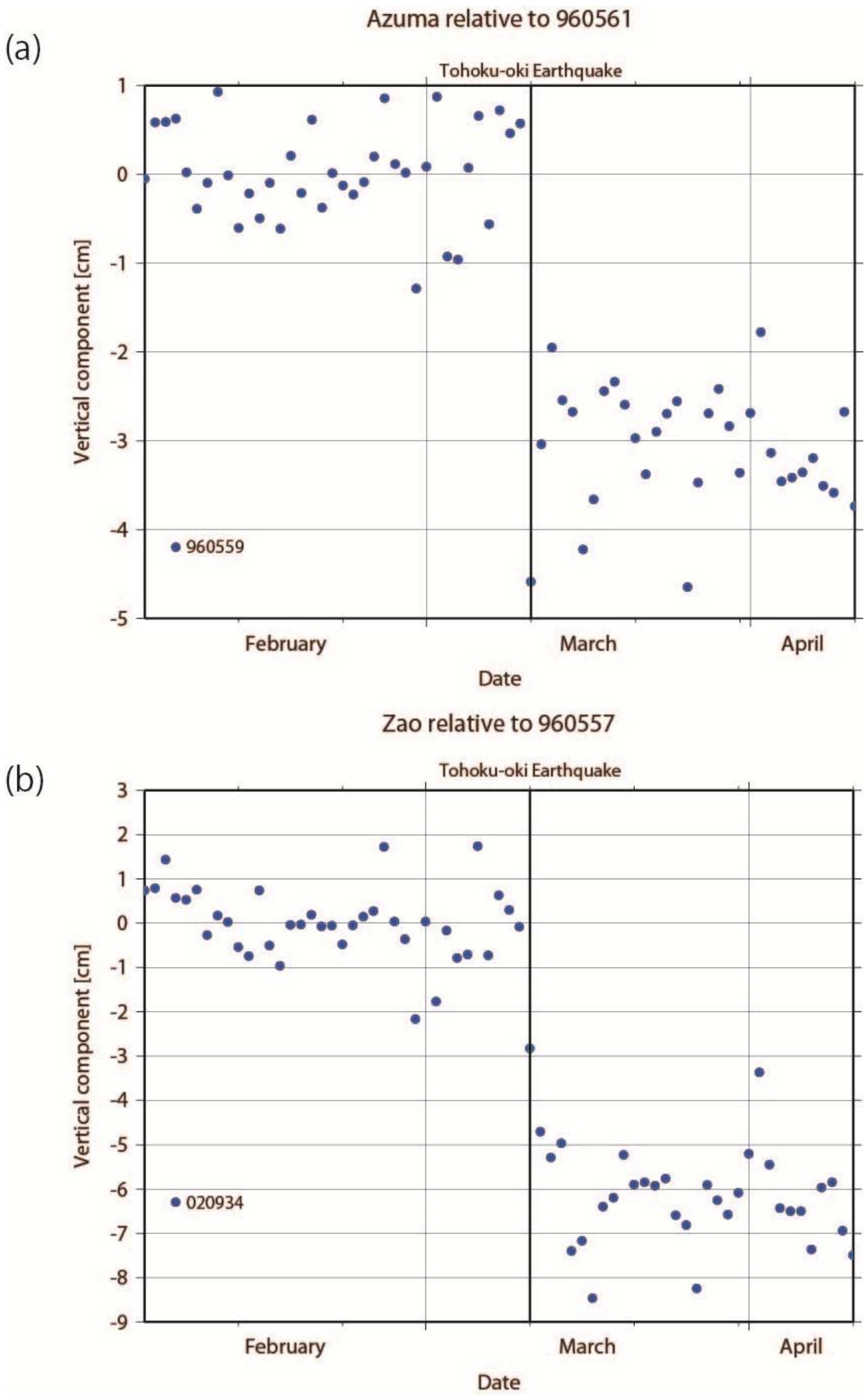

Supplementary Fig. 4. Time series of GPS-derived vertical displacements without moving average for the stations indicating remarkable subsidence. All values are relative to the reference station. Data are from GEONET F3 solution published by the Geospatial Information Authority of Japan (GSI).
(a) Azuma region. (b) Zao region. The reference station is 960561 for (a) (Supplementary Fig. 2d) and 960557 for (b) (Fig. 1d). The thick black line indicates the timing of the mainshock on 11 March 2011.

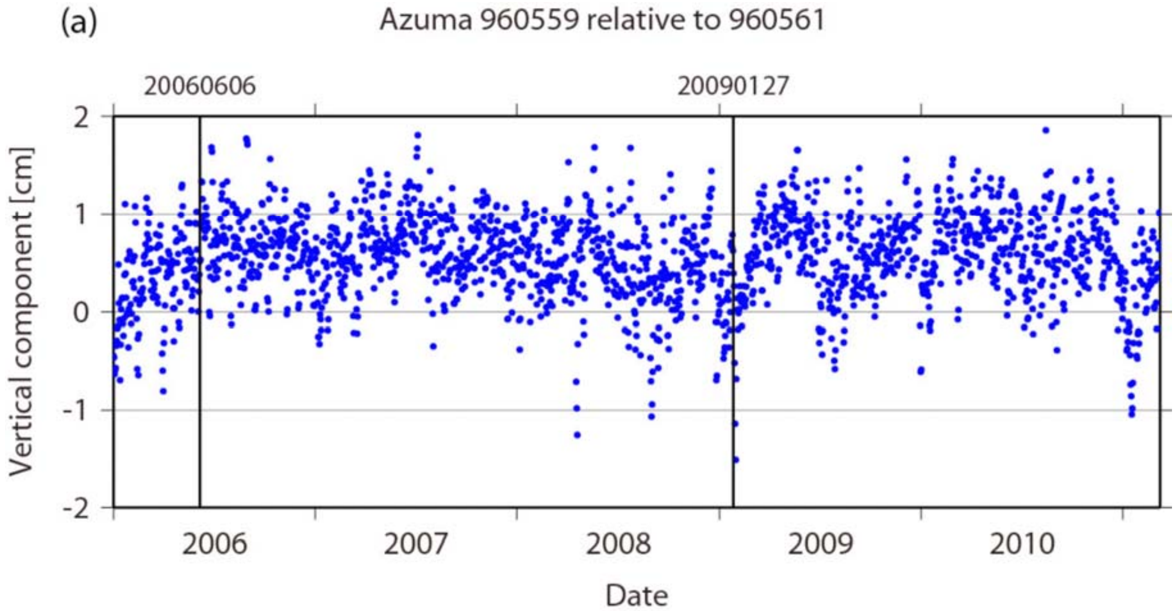

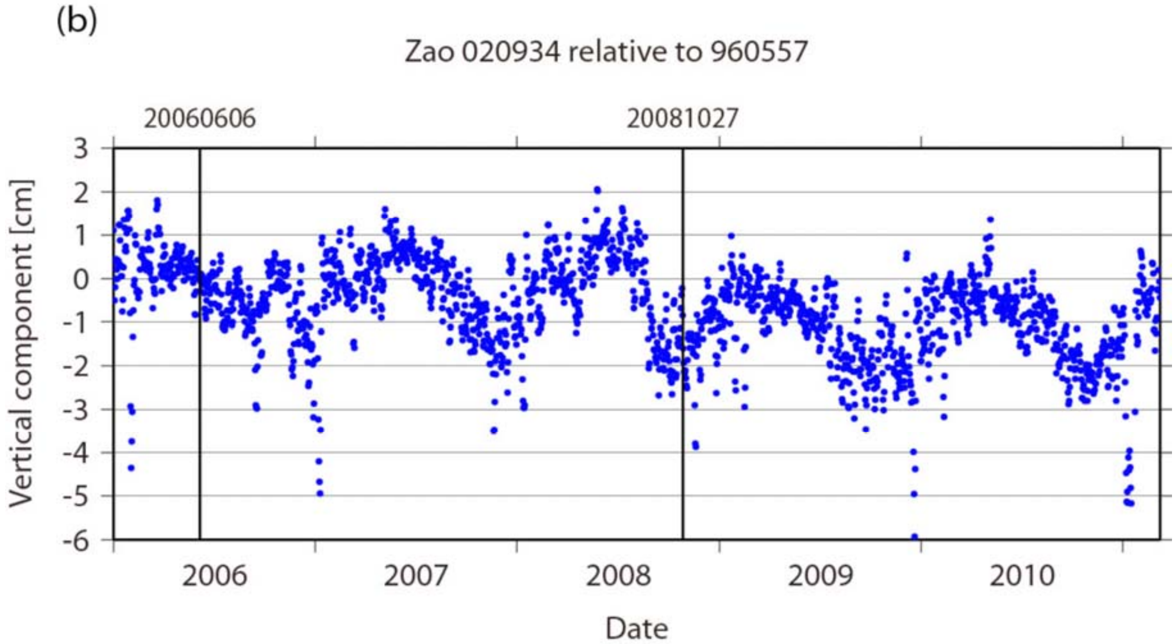

Supplementary Fig. 5. Time-series of GPS vertical displacements from 1 Jan. 2006 to 10 Mar. 2011 at stations located within the deformed region relative to a reference station located outside. (a) Mt. Azuma. (b) Mt. Zao. See Fig. 1d and e for the locations of the stations. Two vertical lines in each subset denote the first and second acquisition dates of the interferograms that contained localized signals. No more than a few centimeters of vertical displacements are indicated within this period, showing the lack of subsidence signals larger than the noise level.

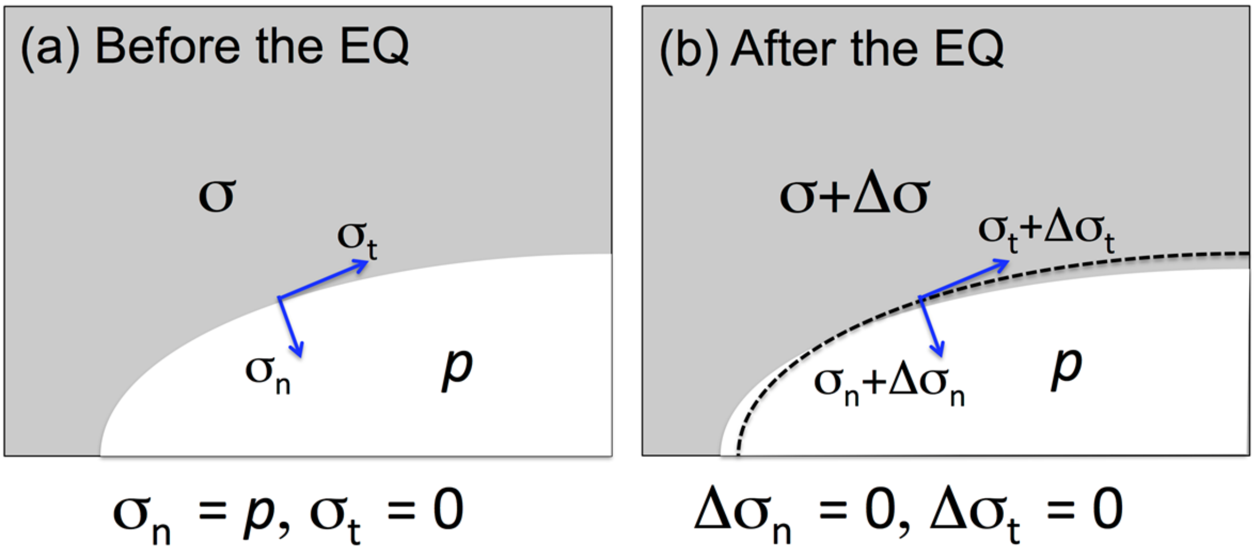

Supplementary Fig. 6. Schematic figures showing the boundary conditions on the surface of the ellipsoid. (a) Before the earthquake. The normal stress $\boldsymbol{\sigma_n}$ on the ellipsoidal surface is balanced with the pressure *p*, and the tangential stress is zero. (b) After the earthquake, stress changes $\Delta\boldsymbol{\sigma}$ is given. The change in the inner pressure is neglected. The boundary conditions on the ellipsoidal surface are such that the changes in the normal and tangential stresses are zero.

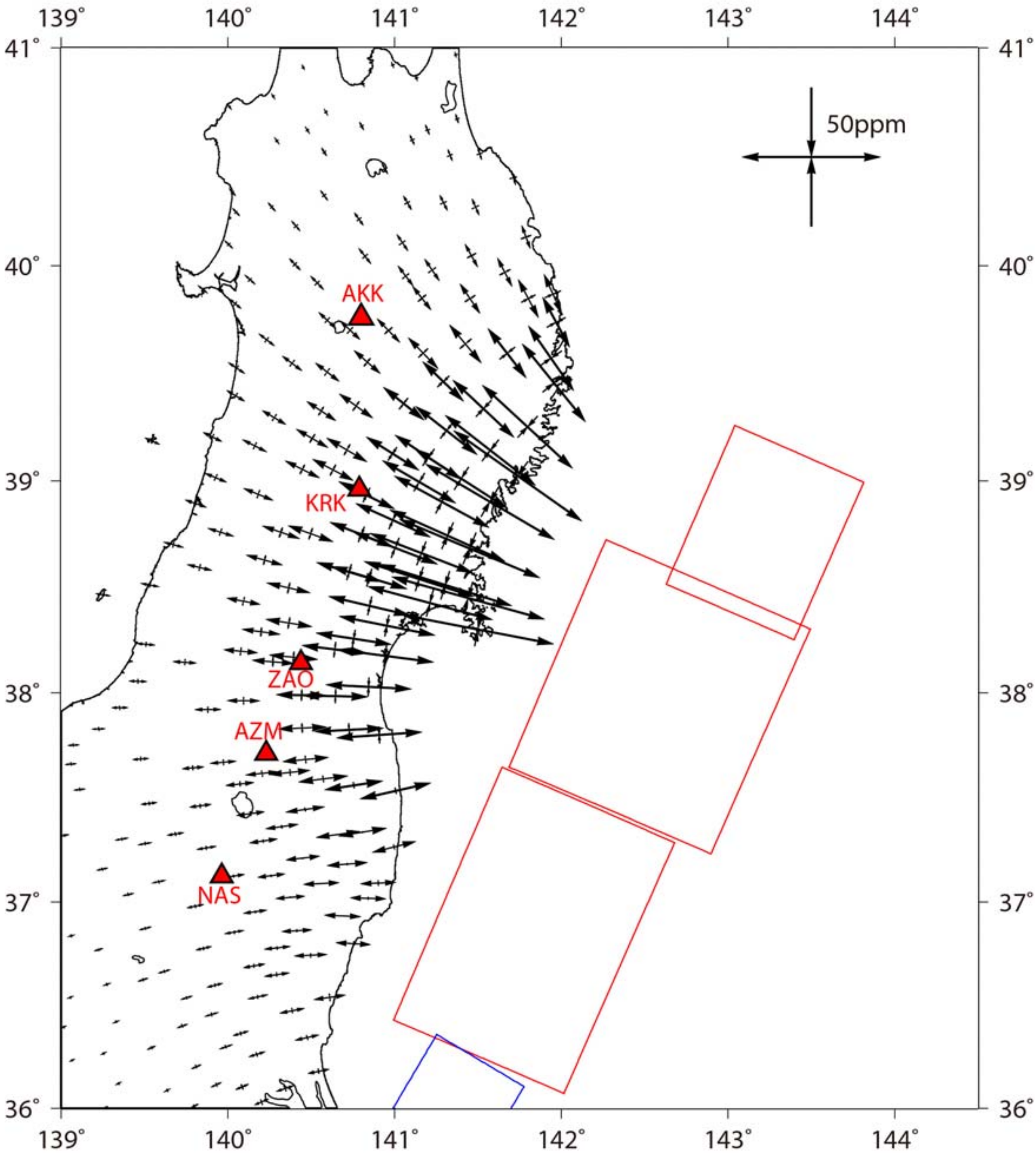

Supplementary Fig. 7. Strain changes at the surface due to a fault model composed of multiple rectangular dislocations[6]. Arrows indicate the principal strain axes. Red and blue rectangles correspond to the fault models of the mainshock and the largest aftershock (Mw 7.7), respectively. AKK, KRK, ZAO, AZM, and NAS stand for Mt. Akitakoma, Mt. Kurikoma, Mt. Zao, Mt. Azuma, and Mt. Nasu, respectively.

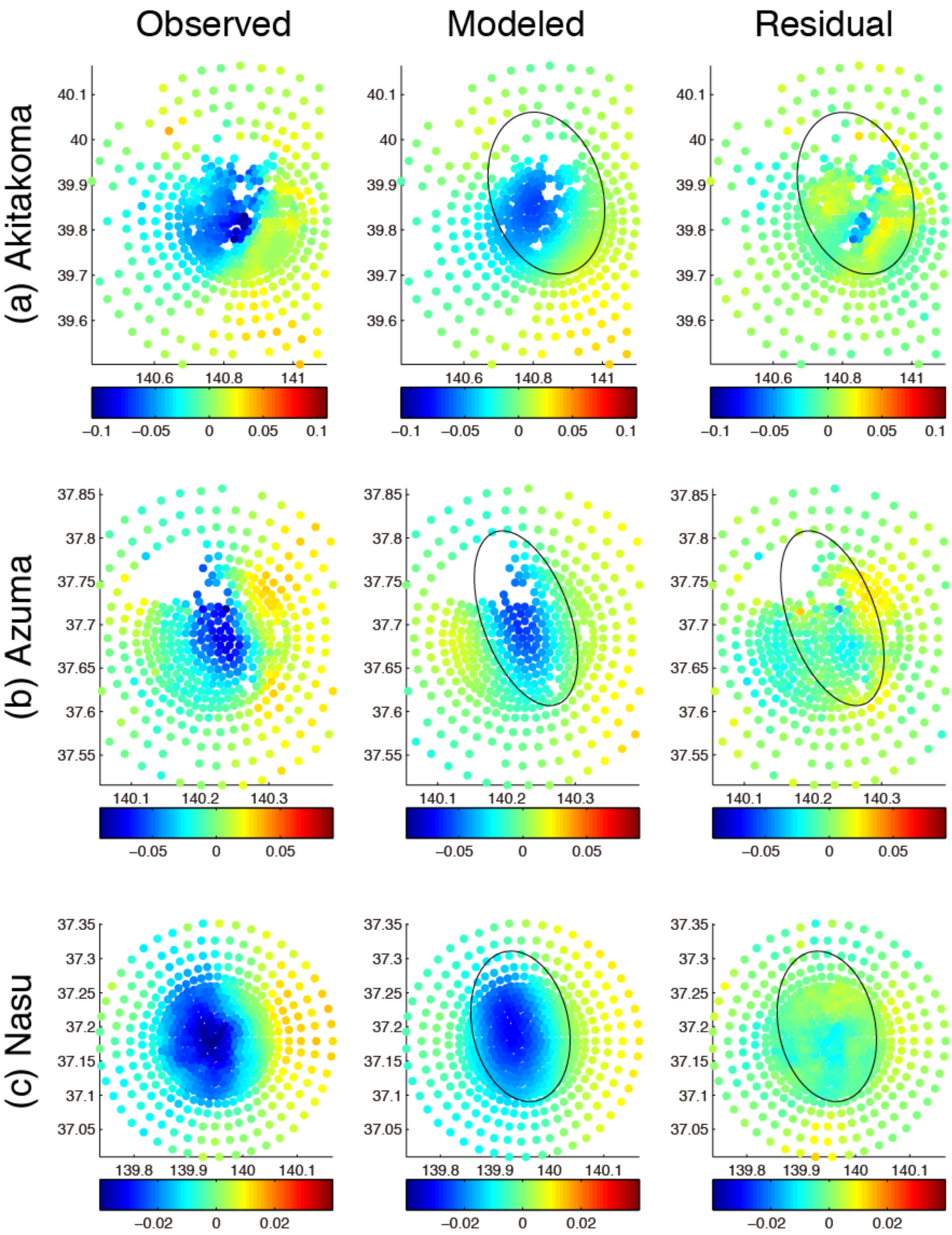

Supplementary Fig. 8. Comparison of observed data used for the inversion (left), modeled data that corresponds to the optimum model (middle), and the residual (right) for the three volcanoes. Black ellipsoid shows the horizontal location of the optimum model. The color shows the LOS displacements in meters.

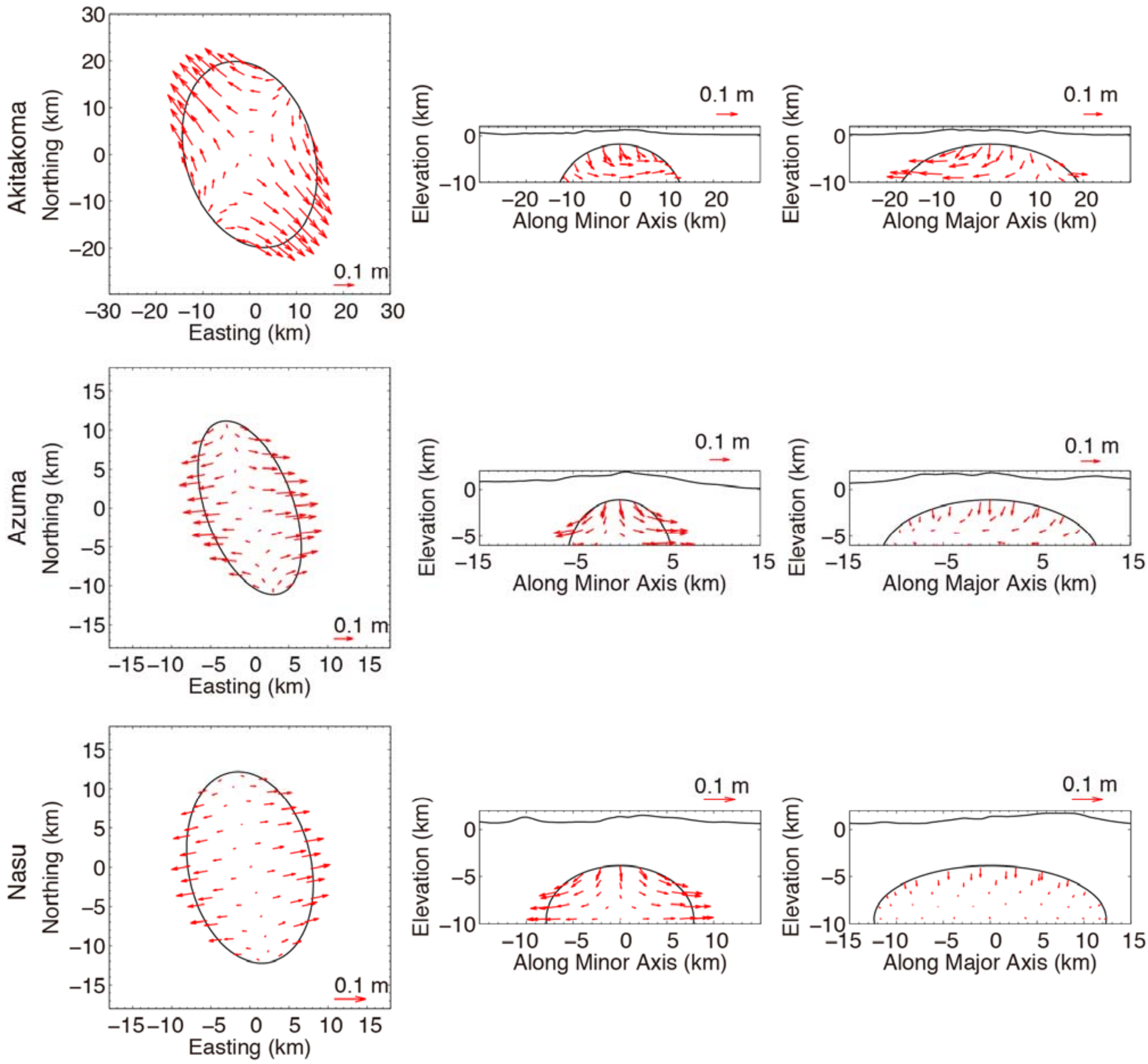

Supplementary Fig. 9. Displacements of the boundary of the optimum ellipsoidal models for the three volcanoes. (Left) Plane view seen from above. (Middle) Cross-sectional view seen from the direction of the major horizontal axis. (Right) Cross-sectional view seen from the direction of the minor horizontal axis. The topography is shown in black curves.

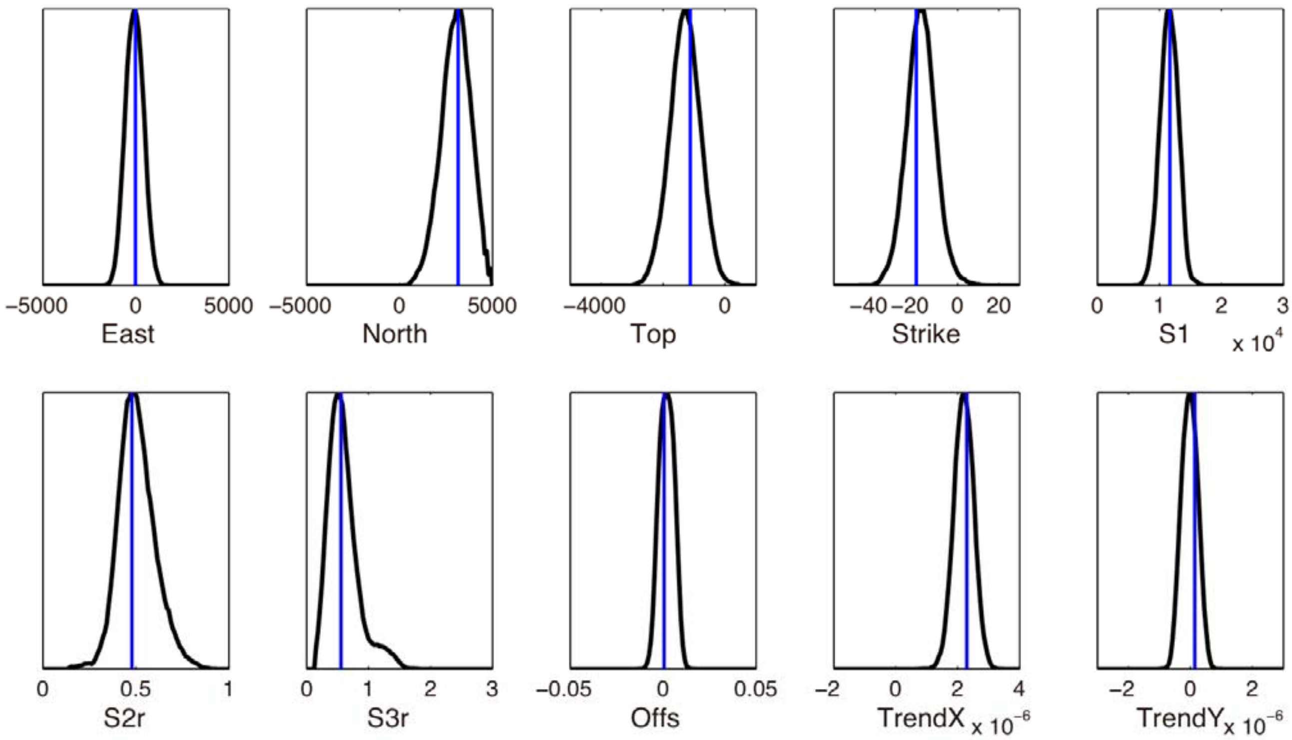

Supplementary Fig. 10. Example of one-dimensional marginal probability density functions. This example is for the inversion on Mt. Azuma data. Blue lines correspond to the optimum model. Refer to Supplementary Table 4 for the meanings of the parameters. The 95% confidence intervals (Supplementary Table 5) are calculated in such a way that, for each parameter, the upper and lower 2.5% of the total area become out of the confidence interval.